UC Berkeley
UC Berkeley Previously Published Works

Title
Thermodynamic accessibility of Li—Mn—Ti—O cation disordered rock-salt phases

Permalink
https://escholarship.org/uc/item/49n280wk

Journal
Journal of Materials Chemistry A, 14(51)

ISSN
2050-7488

Authors
Kam, Ronald L
Wang, Shilong
Ceder, Gerbrand

Publication Date
2026-08-27

DOI
10.1039/d6ta03748h

Copyright Information
This work is made available under the terms of a Creative Commons Attribution License, available at https://creativecommons.org/licenses/by/4.0/

Peer reviewed

eScholarship.org Powered by the California Digital Library
University of California

Journal of Materials Chemistry A

ROYAL SOCIETY OF CHEMISTRY

PAPER

Published on 21 July 2026
Licensed under CC-BY 4.0

Check for updates

Cite this: J. Mater. Chem. A, 2026, 14, 34773

Thermodynamic accessibility of Li–Mn–Ti–O cation disordered rock-salt phases

Ronald L. Kam, †[ab] Shilong Wang †[ab] and Gerbrand Ceder *[ab]

Disordered rock-salt (DRX) cathodes within the Li–Mn–Ti–O (LMTO) composition space have recently been extensively studied, as they promise to deliver exceptional energy density at low cost in Li-ion batteries. The development of LMTO DRX with improved electrochemical performance requires optimization of the composition and particle size/morphology, which are determined by synthesis conditions such as annealing temperature. These challenges motivate an investigation of the LMTO rock-salt phase diagram, with a focus on understanding the stability of DRX by quantifying the order-disorder transition temperature (T_{disord}) as a function of composition. First-principles calculations and X-ray diffraction experiments are applied to establish the LMTO phase diagram, which lies within the $LiMnO_2$–Li_2MnO_3–Li_2TiO_3 pseudo-ternary. The T_{disord} decreases significantly as off-stoichiometry is introduced to the end-point compositions, resulting in a eutectoid phase diagram. Importantly, a significant range of LMTO compositions containing small to moderate fractions of Li-excess and Ti^{4+} doping (relative to $LiMnO_2$) have T_{disord} spanning 700–900 °C. These temperatures are substantially lower than conventional DRX synthesis temperatures, suggesting the promise of decreasing synthesis temperatures for specific DRX compositions. The compositions containing moderate to high fractions of Mn^{4+} instead have greater T_{disord} and phase separation to layered Li_2MnO_3 becomes highly favored.

Received 4th May 2026
Accepted 6th July 2026

DOI: 10.1039/d6ta03748h

rsc.li/materials-a

1 Introduction

Lithium-ion (Li) batteries have been instrumental towards the rapid growth in electric vehicles, grid-scale energy storage, and personal electronic devices.[1–3] The projected rise in Li battery demand in the next decades necessitates the continued development of battery chemistries that utilize inexpensive and earth-abundant elements.[3,4] Cation disordered rock-salt with Li-excess (DRX) cathode materials are a particularly promising class of Li cathode materials that utilize earth abundant elements and can deliver high energy density that rivals state-of-the-art Ni–Mn–Co (NMC) cathodes.[5–10] The Li–Mn–Ti–O (LMTO) composition space has been a fruitful source of candidate DRX compositions, such as $Li_{1.2}Mn_{0.4}Ti_{0.4}O_2$ and $Li_{1.05}Mn_{0.85}Ti_{0.1}O_2$.[5,6,8,9,11–15]. More recently, it has been found that Mn-rich LMTO compositions such as $Li_{1.05}Mn_{0.85}Ti_{0.1}O_2$ are especially promising, as they tend to transform to δ-DRX phases with anti-phased nanoscale spinel domains upon electrochemical cycling or chemical delithiation, leading to improved power density.[5,14,16–18]

DRX compositions with high Mn fraction are typically prepared using conventional solid-state synthesis at relatively high temperatures ≥1000 °C.[6–8,15] Recently, Patil *et al.* showed that LMTO DRX compositions containing relatively higher fractions of Li and Ti, such as $Li_{1.2}Mn_{0.4}Ti_{0.4}O_2$, can be prepared at lower temperatures ∼ 800 °C through sol–gel synthesis.[15] Other strategies such as molten-salt[19] and microwave synthesis[20] have also been developed. The synthesis conditions have a strong impact on particle size and short-range order, which in turn affect the electrochemical kinetics of (δ)-DRX.[5,17] For example, at high temperature the particles can grow very quickly and inhomogeneously, leading to poor electrochemical kinetics.[17] Thus, it is favorable to lower DRX synthesis temperatures, as well as optimize other synthesis conditions such as the holding times and heating/cooling rates. It becomes vital then to understand the minimum temperatures at which DRX becomes thermodynamically stabilized (*i.e.* the order–disorder transition temperature—which we will refer to as T_{disord}), and assess the possible composition dependence of T_{disord}.

Since DRX is a disordered phase, it is expected to be stabilized at elevated temperature by its increased configurational entropy (S_{config}). Meanwhile, the enthalpic (H) contribution to the free energy is more favorable for the ordered ground states. The balance between S_{config} and H contributions determines the T_{disord} and stability of DRX relative to the ordered phases. The S_{config} can be significantly influenced by the number of distinct species and their fractions present within a given composition,

[a]Department of Materials Science and Engineering, University of California, Berkeley, CA 94720, USA. E-mail: gceder@berkeley.edu

[b]Materials Science Division, Lawrence Berkeley National Laboratory, Berkeley, CA 94720, USA

† These authors contributed equally to this work.

as well as the tendency of certain species to form short-range order. The enthalpy of DRX can be significantly lowered by adding ions with the d^0 electron configuration (such as Ti^{4+}), since the d^0 electronic structure can accommodate local lattice distortions at minimal energy cost, as previously shown by Urban *et al.*[21]

The objective of our study is to derive a phase diagram of LMTO rock-salt-type phases, using a combination of *ab initio* thermodynamics and experiments. As shown in Fig. 1a, we span the pseudo-ternary of $LiMnO_2$–Li_2MnO_3–Li_2TiO_3 compositions. Previous experiments have shown that the ordered phases that are stable at ambient temperature are the orthorhombic $LiMnO_2$ phase,[22–24] layered Li_2MnO_3,[25,26] and layered Li_2TiO_3.[27–29]. The orthorhombic $LiMnO_2$ (*Pmmn*) structure exhibits corrugated layers of Mn or Li that alternate with each other, which we note is unique because other analogous $LiMO_2$ compositions (where *M* can be a single species or an admixture of species) typically crystallize in a layered $R\bar{3}m$ structure.[30] The unique stability of the orthorhombic *Pmmn* structure has been attributed to the cooperative Jahn–Teller (JT) distortion of Mn^{3+} ions, which lowers the total energy by breaking the degeneracy of the single half-filled e_g states of Mn^{3+} ions. In layered Li_2MnO_3, the Mn are nominally in the +4 oxidation state with unfilled e_g states, so they do not exhibit a JT distortion. The layered Li_2MnO_3 and Li_2TiO_3 phases are nearly isostructural in that they consist of alternating planes of Li and D_2Li (where D can either be Mn or Ti), with the D atoms arranged in honeycombs surrounding each Li. Layered Li_2TiO_3 has been reported to crystallize with the *C*2/*c* space group, while Li_2MnO_3 has been reported to have either *C*2/*c* or *C*2/*m* symmetry,[25,26,31] with these differences in symmetry arising from distinct stacking patterns of the honeycomb-ordered D_2Li layers.[26] Within our first-principles calculations, we find that the *C*2/*m* and *C*2/*c* stacking patterns yield nearly identical total energies (within 0.6 meV per atom) for Li_2MnO_3 and Li_2TiO_3, consistent with previous work on Li_2MnO_3.[32]

Since the nominal oxidation states of Mn in $LiMnO_2$ and Li_2MnO_3 are +3 and +4, respectively, the compositions along the $LiMnO_2$–Li_2MnO_3 pseudo-binary (Fig. 1a) are expected to contain Mn^{3+}, Mn^{4+}, and excess Li (relative to $LiMnO_2$) in ratios that preserve charge neutrality, as described by the expression $Li_{1+x}Mn^{3+}_{1-3x}Mn^{4+}_{2x}O_2$, where x is the fraction of excess Li (per O_2) relative to $LiMnO_2$ and spans the range $0 \leq x \leq 1/3$. Compositions along the $LiMnO_2$–Li_2TiO_3 pseudo-binary can be described by an analogous expression $Li_{1+x}Mn^{3+}_{1-3x}Ti^{4+}_{2x}O_2$. The third axis of the LMTO pseudo-ternary is the replacement of Mn^{4+} with Ti^{4+} ($Li_2Mn^{4+}_{1-y}Ti^{4+}_yO_3$ Fig. 1a). Considering all compositional constraints, the LMTO rock-salt compositions can be described by the expression $Li_{1+x}Mn_{1-x-y}Ti_yO_2$, where $0 \leq x \leq \frac{1}{3}$ and $0 \leq y \leq 2x$. All possible structures within the LMTO rock-salt space represent distinct cation arrangements (Li^+, Mn^{3+}, Mn^{4+}, or Ti^{4+}) on a face-centered-cubic (FCC) lattice of octahedral sites. The unit cell of the rock-salt framework is shown in Fig. 1b.

The most important aspect of our study is to understand the stability of the DRX phase by mapping T_{disord} as a function of composition. From first-principles modeling, we account for the electronic and configurational free energy contributions, by harnessing the cluster expansion (CE) and Monte Carlo (MC) sampling approach,[33–35] which have been extensively applied to study the thermodynamics of a wide range of disordered materials systems spanning battery cathodes,[36–38] alloys,[39,40] magnetic materials,[41,42] and more. We train a CE model to describe the energetics of the quaternary configuration space of cation sites (Fig. 1b). We distinguish between the +3 and +4 states of Mn as it has been shown by Zhou *et al.* that the "configurational electronic" entropy of a species in different oxidation states can be critical for stabilizing solid-solution phases in ionic materials such as $Li_xFe^{2+}_xFe^{3+}_{1-x}PO_4$.[43]

To accurately compute the LMTO phase diagram, the CE model must be trained on density-functional theory (DFT)-computed total energies that realistically describe the energetics of the possible structures—and most crucially, reproduce the correct ground states. In a recent study, we have shown that commonly utilized DFT approaches such as GGA (PBEsol[44]) and

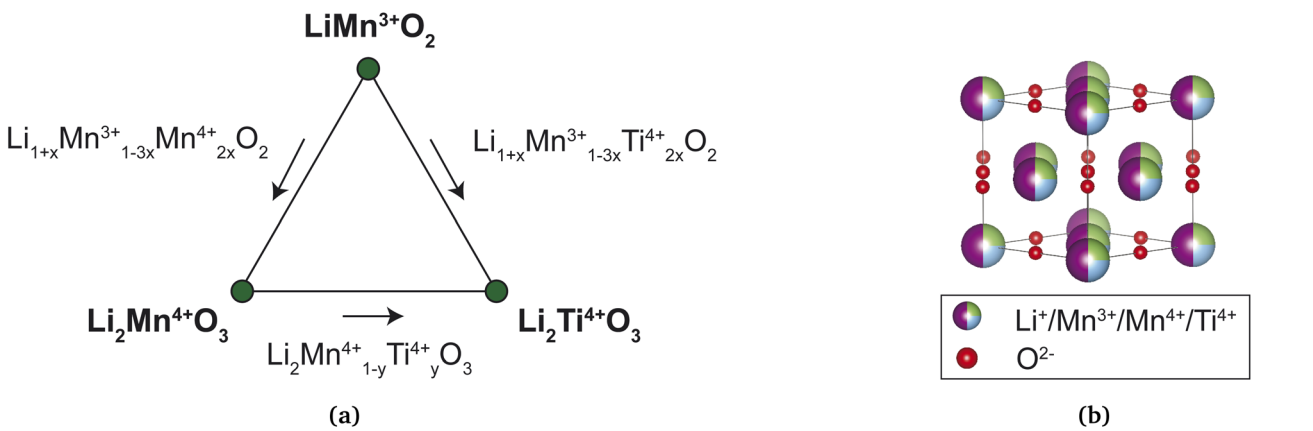


Fig. 1 Composition and configuration space of the LMTO rock-salt phases. (a) Pseudo-ternary $LiMnO_2$–Li_2MnO_3–Li_2TiO_3 composition space. Nominal TM oxidation states and changes in composition along the edge pseudo-binary lines are labeled. (b) Unit cell of the FCC rock-salt lattice, with octahedral cation sites that can be occupied by Li^+, Mn^{3+}, Mn^{4+}, or Ti^{4+}.

 This journal is © The Royal Society of Chemistry 2026

meta-GGA (r^2SCAN[45]) functionals, with or without empirical Hubbard U corrections,[46] spuriously predict the ground state of $LiMnO_2$ to be the γ-$LiMnO_2$ polymorph (isostructural to γ-$LiFeO_2$),[47] which has never been reported in experiment.[48] Meanwhile, the HSE06 hybrid-GGA functional[49] can correctly predict the orthorhombic phase to be the $LiMnO_2$ ground state. Thus, we use HSE06 to calculate the total energy of each structure to train our CE model (more details in Section 4.1). We note that HSE06 requires significantly more computational resources compared to GGA and *meta*-GGA functionals, which is the main reason why most previous studies involving DFT and CE calculations of LMTO phases have employed GGA or *meta*-GGA-based techniques.[36–38] The failures of the PBEsol and r^2SCAN-based methods to predict the correct $LiMnO_2$ ground state properties have been attributed to the complex interplay between JT distortions, electronic localization, and antiferromagnetism of Mn^{3+} ions, which the HSE06 functional can capture with better accuracy due to the more precise treatment of screened electronic exchange interactions within the hybrid-GGA formalism.[48] This helps reduce self-interaction and delocalization errors within DFT that can be large when treating correlated 3d electron states.[46,49,50] Furthermore, accounting for AFM order was shown in previous studies to significantly lower the energy of each $LiMnO_2$ phase compared to the ferromagnetic (FM) state and improve $LiMnO_2$ phase stability predictions,[48,51] so we also search for the lowest energy AFM ordering for each ion configuration within PBEsol + U, using a previously developed DFT workflow.[52,53]

By calculating the energies of each LMTO structure using the HSE06 functional (more details in Section 4.1), we can reasonably capture the complex electronic structure of the LMTO phases (especially near the $LiMnO_2$ composition) and curate a DFT data set that contains the physically correct ground states. A CE model is parameterized on this DFT data, which recovers the known LMTO ground states. The CE is then harnessed to perform MC sampling and thermodynamic integration to compute the free energies of the competing ordered and disordered LMTO phases, and determine the phase boundaries between them (more details in Methods).

We perform a complementary set of experiments utilizing heating and *in situ* X-ray diffraction (XRD) measurements within an inert environment to track the phase evolution as a function of temperature for specific LMTO compositions along the $LiMnO_2$–Li_2TiO_3 and $LiMnO_2$–Li_2MnO_3 pseudo-binary composition axes (Fig. 1a). For each composition, we quantify the temperature at which DRX becomes phase-pure (which we define as T_{disord}) and identify the ordered phases that form below T_{disord}. The experiments are performed under an inert environment to prevent oxidation of the samples, which can lead to the formation of undesired phases such as spinel $LiMn_2O_4$.[54,55]. A similar heating and *in situ* XRD set-up has recently been used by Liang *et al.* to rationalize the reaction mechanisms leading to DRX formation in the fluorinated $Li_{1.1}Mn_{0.8}Ti_{0.1}O_{1.9}F_{0.1}$ composition.[56] We also perform quenching of select compositions from temperatures near T_{disord}.

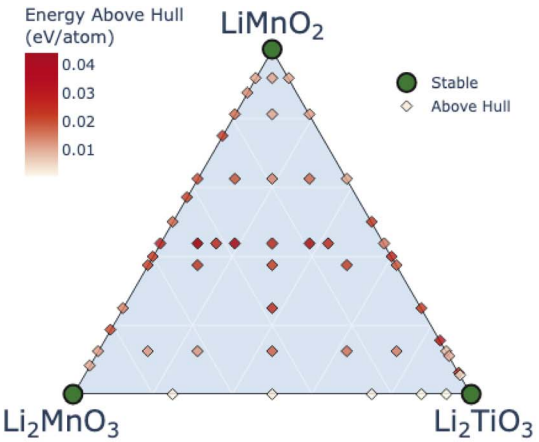
We identify the LMTO phase diagram to be a eutectoid-like phase diagram, in which the T_{disord} decreases upon introducing off-stoichiometry to the end-point phases (orthorhombic $LiMnO_2$, layered Li_2TiO_3, and layered Li_2MnO_3). Importantly, introducing small to moderate amounts of Li-excess, Ti^{4+}, and/or Mn^{4+} (relative to $LiMnO_2$) can lead to T_{disord} values that are significantly lower than typically used DRX synthesis temperatures (≥1000 °C). In general, the results of our calculations agree well with experiments. However, in experiments on compositions with a small amount of Li excess compensated by Mn^{4+}, we observe a layered $LiMnO_2$-like phase to form. Our calculations do not predict this phase to be thermodynamically stable, suggesting it is a metastable phase that can form more rapidly than the thermodynamically predicted phase separation upon cooling.

2 Results

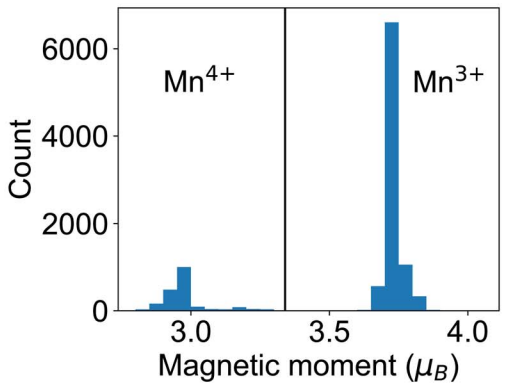
To construct our DFT dataset of LMTO rock-salt structures, we enumerate structures across the pseudo-ternary $LiMnO_2$–Li_2MnO_3–Li_2TiO_3 composition space, with the sampled compositions shown in Fig. 2a. Many of these structures were generated by introducing off-stoichiometry and/or anti-site defects to the ordered LMTO ground states (orthorhombic $LiMnO_2$, layered Li_2MnO_3, layered Li_2TiO_3), as well as other low-energy ordered $LiMnO_2$ phases such as layered, spinel, and γ-$LiMnO_2$. Disordered configurations are also sampled from MC simulations at elevated T across various LMTO compositions. An internal database of LMTO rock-salt structures compiled in previous studies is also used.[36–38] In all, we gather 745 unique cation configurations in the LMTO rock-salt lattice and calculate their formation energies at $T = 0$ K using the HSE06 hybrid-GGA functional. The compositions and energies are shown as color-coded squares in Fig. 2a. With the exception of the end-point ground state phases, we do not identify any additional LMTO structures that are predicted to be stable at $T = 0$ K from DFT, as all enumerated structures have positive energies above the hull (E_{hull}).

To provide a more quantitative visualization of the energy landscape, we plot the formation energies along the pseudo-binary $LiMnO_2$–Li_2TiO_3 ($Li_{1+x}Mn^{3+}_{1-3x}Ti^{4+}_{2x}O_2$) and $LiMnO_2$–Li_2MnO_3 ($Li_{1+x}Mn^{3+}_{1-3x}Mn^{4+}_{2x}O_2$) axes in Fig. 2c and d, respectively. The $Li_{1+x}Mn^{3+}_{1-3x}Ti^{4+}_{2x}O_2$ structures can have significantly lower values of E_{hull} compared to the $Li_{1+x}Mn^{3+}_{1-3x}Mn^{4+}_{2x}O_2$ space. For example, there are many $Li_{1+x}Mn^{3+}_{1-3x}Ti^{4+}_{2x}O_2$ structures with $E_{hull} \lesssim 10$ meV per atom, while there are no $Li_{1+x}Mn^{3+}_{1-3x}Mn^{4+}_{2x}O_2$ structures with $E_{hull} < 10$ meV per atom. The structures with lowest E_{hull} are the layered $LiMnO_2$, orthorhombic $LiMnO_2$, γ-$LiMnO_2$, spinel $LiMnO_2$, and layered Li_2MnO_3/Li_2TiO_3 phases with off-stoichiometry.

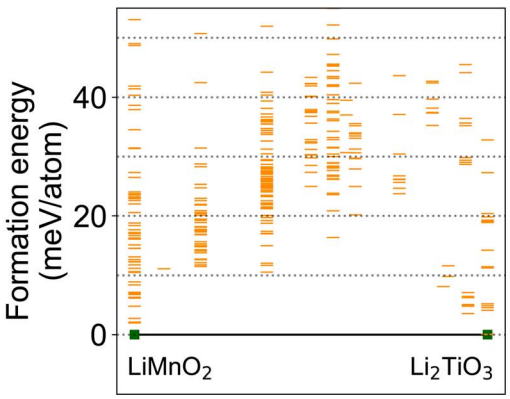
We assign oxidation states to the Mn atoms in each LMTO structure based on the absolute values of the Mn magnetic moments ($|m_{Mn}|$) computed within HSE06, a histogram of which is shown in Fig. 2b. We find a clearly bimodal distribution of $|m_{Mn}|$ with peaks centered at $|m_{Mn}| = 3.0$ and 3.7 μ_B. By assigning all higher spin Mn with $|m_{Mn}| > 3.35$ μ_B to be Mn^{3+} and Mn with $|m_{Mn}| \leq 3.35$ μ_B to be Mn^{4+}, the number of structures that are formally charge-neutral is maximized.[36] The average $|m_{Mn}|$ of Mn^{3+} and Mn^{4+} that we calculate within the HSE06 functional are in reasonable agreement with previous



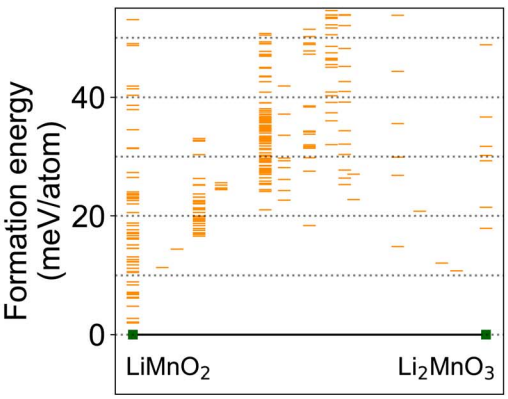
(a) Formation energies of LMTO pseudo-ternary



(b) Mn magnetic moments



(c) Formation energies of $Li_{1+x}Mn^{3+}_{1-3x}Ti^{4+}_{2x}O_2$



(d) Formation energies of $Li_{1+x}Mn^{3+}_{1-3x}Mn^{4+}_{2x}O_2$

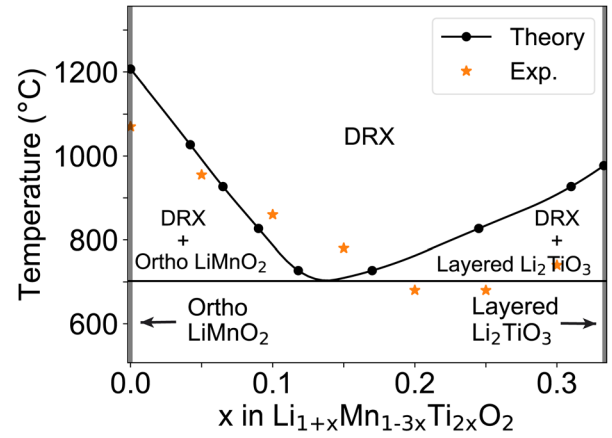
Fig. 2 DFT-computed formation energies at 0 K and Mn magnetic moments of the training set of LMTO rock-salt orderings. (a) Formation energies of structures within the LMTO pseudo-ternary—specifically the lowest energies of each sampled composition. Green circles represent stable phases and squares represent configurations with energy above the convex hull. (b) Histogram of absolute values of Mn magnetic moments ($|m_{Mn}|$). The vertical line at $|m_{Mn}| = 3.35\ \mu_B$ denotes the threshold between Mn^{3+} and Mn^{4+}, with all Mn with $|m_{Mn}| > 3.35\ \mu_B$ assigned to be Mn^{3+}, while Mn with $|m_{Mn}| < 3.35$ assigned as Mn^{4+}. Formation energies along the pseudo-binary (c) $LiMnO_2$–Li_2TiO_3 ($Li_{1+x}Mn^{3+}_{1-3x}Ti^{4+}_{2x}O_2$) and (d) $LiMnO_2$–Li_2MnO_3 ($Li_{1+x}Mn^{3+}_{1-3x}Ti^{4+}_{2x}O_2$) composition lines, where green squares are stable phases and orange lines are configurations above the convex hull.

studies[33,36] that utilized *meta*-GGA (SCAN or r^{2}SCAN) functionals, though our $|m_{Mn}|$ values computed within HSE06 are systematically slightly higher and the distribution more discrete (less continuous). These differences in our calculated $|m_{Mn}|$ compared to previous studies can be attributed to the reduced self-interaction error (SIE) of the HSE06 hybrid-GGA functional, which helps enforce greater electron localization onto the Mn-3d states compared to *meta*-GGA methods. The calculated magnetic moments of all Ti atoms are near zero (within 0.01 μ_B), which confirms that all Ti are in the +4 oxidation state.

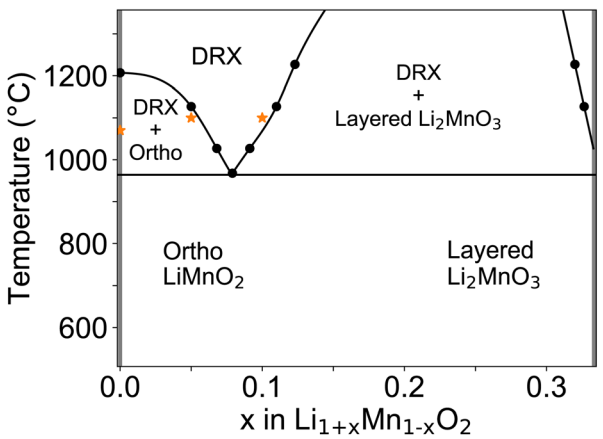
To understand the phase stability at elevated temperature, we parametrize a CE on the DFT energies of the LMTO rock-salt structures and perform MC simulations and thermodynamic integration to map the phase diagram of this system. Our trained CE model correctly recovers the DFT-predicted ground states, as shown in SI Fig. S1. We specifically analyze the pseudo-binary spaces of $LiMnO_2$–Li_2TiO_3 ($Li_{1+x}Mn^{3+}_{1-3x}Ti^{4+}_{2x}O_2$), $LiMnO_2$–Li_2MnO_3 ($Li_{1+x}Mn^{3+}_{1-3x}Mn^{4+}_{2x}O_2$), and $LiMnO_2$–$Li_2Mn_{0.5}Ti_{0.5}O_3$ ($Li_{1+x}Mn^{3+}_{1-3x}Mn^{4+}_{2x}Ti^{4+}_xO_2$). By examining these select pseudo-binary systems, we can quantitatively analyze the influence of Li-excess (x) and type/concentration of the +4 ion (which we will refer to as D^{4+}, where D can either be Mn or Ti) towards stabilizing the DRX phase. We calculate the temperature–composition phase diagrams of $Li_{1+x}Mn^{3+}_{1-3x}Ti^{4+}_xO_2$, $Li_{1+x}Mn^{3+}_{1-3x}Mn^{4+}_{2x}O_2$, and $Li_{1+x}Mn^{3+}_{1-3x}Mn^{4+}_xTi^{4+}_xO_2$, and plot them along with the T_{disord} determined from *in situ* XRD experiments (gold stars) in Fig. 3. The *in situ* XRD heatmaps of each composition are shown in SI Fig. S2.

Within the $Li_{1+x}Mn^{3+}_{1-3x}Ti^{4+}_{2x}O_2$ pseudo-binary phase diagram (Fig. 3a), the calculated T_{disord} of $LiMnO_2$ is 1200 °C, which is in reasonable agreement with experiment (1070 °C). As the Li and Ti concentration increases, T_{disord} linearly decreases until a predicted eutectoid point at $T_{eutec} = 700$ °C and $x_{eutec} = 0.14$ ($Li_{1.14}Mn_{0.58}Ti_{0.28}O_2$). The experimental DRX phase boundary in this composition range is also linearly sloped, though the decrease of T_{disord} within experiment is less pronounced compared to the simulations. The experimental eutectoid point is projected to be

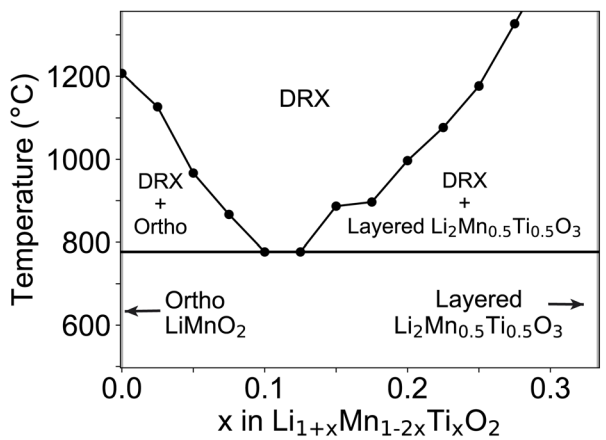
 This journal is © The Royal Society of Chemistry 2026



(a) $LiMnO_2 - Li_2TiO_3$



(b) $LiMnO_2 - Li_2MnO_3$



(c) $LiMnO_2 - Li_2Mn_{0.5}Ti_{0.5}O_3$

Fig. 3 Temperature–composition phase diagrams of the pseudo-binary composition spaces of (a) $LiMnO_2$–Li_2TiO_3, (b) $LiMnO_2$–Li_2MnO_3, and (c) $LiMnO_2$–$Li_2Mn_{0.5}Ti_{0.5}O_3$, calculated from MC simulations (black lines). Gold stars represent T_{disord} determined from *in situ* XRD experiments, which were performed for select compositions along the $LiMnO_2$–Li_2TiO_3 and $LiMnO_2$–Li_2MnO_3 pseudo-binaries only.

near the temperature $T_{eutec,exp} = 680$ °C and composition $x_{eutec,exp}$ ~ 0.2–0.25 ($Li_{1.2}Mn_{0.4}Ti_{0.4}O_2$ to $Li_{1.25}Mn_{0.25}Ti_{0.5}O_2$). Thus, the experimental and calculated eutectoid temperatures are in reasonable agreement, while the experimental eutectoid composition is higher in Li and Ti concentration than the calculated value. Adding more Li and Ti past x_{eutec} leads to a linear increase in the calculated T_{disord} until the Li_2TiO_3 end-point (Fig. 3a). The experiments show an increase in T_{disord} at $x > x_{eutec,exp}$ as well. Specifically, the experimentally measured T_{disord} of $Li_{1.3}Mn_{0.1}Ti_{0.6}O_2$ is 60 °C higher than that of $Li_{1.25}Mn_{0.25}Ti_{0.5}O_2$. The increase of T_{disord} at high Ti content is consistent with the fact that the reported T_{disord} values of Li_2TiO_3 range from 1155–1200 °C,[28,29] which is higher than our experimentally obtained $T_{eutec,exp}$ (680 °C).

To understand the differences in phase stability when Ti^{4+} is replaced with Mn^{4+}, we examine the $Li_{1+x}Mn^{3+}_{1-3x}Mn^{4+}_{2x}O_2$-pseudo-binary, as shown in Fig. 3b. The trends predicted by theory near the $LiMnO_2$ composition, specifically within the composition range $0 < x < 0.1$, are similar to those observed for $Li_{1+x}Mn^{3+}_{1-3x}Ti^{4+}_{2x}O_2$ (Fig. 3a) in which T_{disord} decreases as a function of x. The predicted eutectoid point of $Li_{1+x}Mn^{3+}_{1-3x}Mn^{4+}_{2x}O_2$ is at $T_{eutec} = 970$ °C and $x_{eutec} = 0.08$ ($Li_{1.08}Mn_{0.92}O_2$ or $Li_{1.08}Mn_{0.76}{}^{3+}Mn_{0.16}{}^{4+}O_2$–Fig. 3b), which is at significantly higher T_{eutec} and lower x_{eutec} than for the Ti^{4+} system. At $x > 0.08$, the T_{disord} rapidly increases as a function of x, leading to a prominent DRX-layered Li_2MnO_3 two-phase region. The dominant factor leading to this wider two-phase region is the high predicted T_{disord} of Li_2MnO_3 (>2800 °C), which is significantly higher than the simulated T_{disord} of Li_2TiO_3 (1000 °C). Thus, the layered Li_2MnO_3 phase is predicted to be very stable and competes strongly with DRX at typical DRX synthesis temperature ranges (~1000 °C), significantly reducing the range of $Li_{1+x}Mn^{3+}_{1-3x}Mn^{4+}_{2x}O_2$ DRX compositions that are accessible at reasonable temperatures.

Our experimentally determined T_{disord} of $Li_{1.05}Mn_{0.95}O_2$ and $Li_{1.1}Mn_{0.9}O_2$ are nearly identical at 1100 °C, in excellent agreement (within ±50 °C) with the computed DRX phase boundary (Fig. 3b). We have performed *in situ* XRD experiments at higher Li and Mn^{4+} concentration, specifically at $x = 0.15$, 0.2, 0.25, and 0.3, from which we could not determine T_{disord} because the temperature at which DRX becomes phase-pure could not be reached due to our furnace's maximum temperature of 1100 °C (SI Fig. S2), indicating that the T_{disord} exceeds this temperature, which is consistent with Fig. 3b. At 1100 °C, the products consist of DRX and layered Li_2MnO_3 phases, as expected from the calculated two-phase region. Thus, although we could not experimentally quantify T_{disord} at these compositions, we confirm that these T_{disord} are very high and thus validate our prediction of a wide DRX-layered Li_2MnO_3 miscibility gap.

To understand the effect of combining Mn^{4+} and Ti^{4+} on phase stability, we calculate the pseudo-binary phase diagram between $LiMnO_2$–$Li_2Mn_{0.5}Ti_{0.5}O_3$ which contains an equal fraction of Mn^{4+} and Ti^{4+} ($Li_{1+x}Mn^{3+}_{1-3x}Mn^{4+}_{x}Ti^{4+}_{x}O_2$), and is shown in Fig. 3c. Unlike the systems shown in Fig. 3a and b, the phase diagram in Fig. 3c is currently based solely on first-principles calculations and has not been experimentally validated yet. Within $Li_{1+x}Mn^{3+}_{1-3x}Mn^{4+}_{x}Ti^{4+}_{x}O_2$, there is a rapid decrease in T_{disord} at low x until the eutectoid point of T_{eutec} ~ 770 °C and x_{eutec} ~ 0.11 ($Li_{1.11}Mn_{0.78}Ti_{0.11}O_2$), which is comparable to the eutectoid point in the $Li_{1+x}Mn^{3+}_{1-}$

$_{3x}Ti^{4+}_{2x}O_2$ system (Fig. 3a). In fact, the DRX phase boundary in the region of $x < 0.11$ is nearly identical to the $Li_{1+x}Mn^{3+}_{1-3x}Ti^{4+}_{2x}O_2$-system (Fig. 3a), which is consistent with a purely entropy-driven increase in the stability of the DRX phase. At higher x, there is a prominent two-phase region between DRX and layered $Li_2Mn_{0.5}Ti_{0.5}O_3$, though this region is significantly smaller than the one between DRX and layered Li_2MnO_3 (shown in Fig. 3b). Thus, the partial substitution of Mn^{4+} with Ti^{4+} increases the accessible composition range of DRX at $900 < T < 1200$ °C. With their relatively low disorder temperatures and high theoretical capacities associated with Mn redox, compositions within the $Li_{1+x}Mn^{3+}_{1-3x}Mn^{4+}_xTi^{4+}_xO_2$ space are promising candidates for battery applications. Their synthesis, structural characteristics, and electrochemical performance will be systematically investigated in future work. We predict the T_{disord} of $Li_2Mn_{0.5}Ti_{0.5}O_3$ to be quite high (~1900 °C), which rationalizes why the two-phase region between DRX and layered $Li_2Mn_{0.5}Ti_{0.5}O_3$ is still relatively large. An important contribution to the stability of layered $Li_2Mn_{0.5}Ti_{0.5}O_3$ is the configurational entropy (S_{config}) of mixing Mn^{4+} and Ti^{4+} within this phase, which significantly lowers the free energy (SI Fig. S3). Meanwhile, the S_{config} in layered Li_2MnO_3 and Li_2TiO_3 is found to be negligible up to their transition temperature, since they exhibit a first-order transition to the disordered state (SI Fig. S4).

To experimentally investigate the miscibility regions of the LMTO phase diagram, we perform *ex situ* XRD characterization of several samples quenched from above and below the respective T_{disord}. Through this analysis, we also assess the practical feasibility of quenching phase-pure DRX samples near the identified T_{disord}. The *ex situ* XRD patterns of quenched $Li_{1.05}Mn_{0.85}Ti_{0.1}O_2$, $Li_{1.1}Mn_{0.7}Ti_{0.2}O_2$, $Li_{1.25}Mn_{0.25}Ti_{0.5}O_2$, and $Li_{1.3}Mn_{0.1}Ti_{0.6}O_2$ samples are shown in Fig. 4. For the $Li_{1.05}Mn_{0.85}Ti_{0.1}O_2$ (Fig. 4a) and $Li_{1.1}Mn_{0.7}Ti_{0.2}O_2$ (Fig. 4b) compositions, the XRD patterns of samples quenched from 1000 °C and 900 °C, respectively, display only the peaks of a DRX reference, which confirms that phase-pure DRX can be isolated slightly above T_{disord}. Refinement results show that the DRX lattice parameters are 4.17 Å and 4.16 Å for $Li_{1.05}Mn_{0.85}Ti_{0.1}O_2$ and $Li_{1.1}Mn_{0.7}Ti_{0.2}O_2$ (SI Fig. S5), respectively, in agreement with previously reported results from typical solid-state synthesis methods.[14] When these samples are quenched from a temperature slightly below T_{disord}, the XRD pattern contains small impurity peaks that can be ascribed to orthorhombic $LiMnO_2$, in addition to the majority DRX peaks (Fig. 4a and b). The presence of a two-phase mixture of DRX and orthorhombic $LiMnO_2$ validates that the samples quenched from below T_{disord} are in the two-phase coexistence region, as predicted by our first-principles phase diagram of $Li_{1+x}Mn^{3+}_{1-3x}Ti^{4+}_{2x}O_2$ (Fig. 3a). Similarly, for the more Li and Ti-rich compositions, $Li_{1.25}Mn_{0.25}Ti_{0.5}O_2$ (Fig. 4c) and $Li_{1.3}Mn_{0.1}Ti_{0.6}O_2$ (Fig. 4d), which are past the eutectic point, pure DRX can be obtained above T_{disord} while layered Li_2TiO_3 is found to coexist with DRX below T_{disord}. The lattice parameters of the pure $Li_{1.25}Mn_{0.25}Ti_{0.5}O_2$ and $Li_{1.3}Mn_{0.1}Ti_{0.6}O_2$ DRX phases are refined to be 4.14 Å and 4.13 Å, respectively (SI Fig. S6).

Replacing Ti^{4+} with Mn^{4+} leads to markedly different phase behavior. *Ex situ* XRD patterns of $Li_{1.05}Mn_{0.95}O_2$, $Li_{1.1}Mn_{0.9}O_2$, and $Li_{1.25}Mn_{0.75}O_2$ samples, quenched from 1100 °C are shown in Fig. 5. Upon quenching $Li_{1.05}Mn_{0.95}O_2$, the resulting sample is predominantly a DRX phase with minor orthorhombic impurities (Fig. 5). This observation is surprising because our *in situ* XRD patterns show that DRX is phase pure at ~1100 °C (SI Fig. S7). We therefore attribute the presence of the orthorhombic impurity to the quench being too slow. As a result, the quenched samples may reflect the equilibrium phase behavior at lower temperatures, where $Li_{1.05}Mn_{0.95}O_2$ would lie within a predicted two-phase region between orthorhombic $LiMnO_2$ and DRX (Fig. 3b). The orthorhombic phase can form before the high-temperature DRX phase is kinetically frozen. A reduced fraction of the orthorhombic impurity phase is observed for $Li_{1.1}Mn_{0.9}O_2$, with DRX remaining the dominant phase, as indicated by the red XRD pattern in Fig. 5. In contrast, quenching $Li_{1.25}Mn_{0.75}O_2$ from 1100 °C yields a mixture of layered Li_2MnO_3 and DRX, in agreement with the corresponding two-phase region in the computed phase diagram (Fig. 3b).

When quenching $Li_{1.05}Mn_{0.95}O_2$ from a slightly lower temperature of 1000 °C, we identify a third phase in addition to orthorhombic $LiMnO_2$ and DRX. The corresponding XRD pattern is shown in SI Fig. S8. Based on the diffraction pattern, we assign this additional phase to be layered $LiMnO_2$, with possible Li-excess. We note that distinguishing a layered $LiMnO_2$-like phase from a lithiated spinel phase using laboratory XRD is challenging due to significant peak overlap. However, a lithiated spinel phase is considered less likely, as it has not been reported to form by direct high-temperature solid-state synthesis starting from Li_2CO_3 and manganese oxides. Furthermore, we performed first-principles calculations to analyze the stability of these phases, which support the formation of a Li-excess layered phase.

In grand-canonical Monte Carlo (GCMC) simulations, we were unable to observe the formation of a layered phase with composition near $Li_{1.05}Mn_{0.95}O_2$. To rationalize the experimentally observed (*meta*)stability of the Li-excess layered phase, we compare the DFT-computed energies of the layered, orthorhombic, and lithiated spinel phases at the $Li_{1.0625}Mn_{0.9375}O_2$ ($Li_{1.0625}Mn_{0.8125}{}^{3+}Mn_{0.125}{}^{4+}O_2$) composition. Because these phases need to accommodate Li-excess through partial occupancy of the Mn sites, we enumerate symmetrically distinct configurations of Li and Mn on those sites and compute their energy above the hull (E_{hull}), which are shown in Fig. 6a. Though all structures have positive values of $E_{hull} \geq 17$ meV per atom, the layered configurations are lower ($E_{hull} \approx 17$ meV per atom) than the orthorhombic and spinel configurations ($E_{hull} \geq 19$ meV per atom). The favorability of the Li-excess layered phase suggests that the experimentally found impurity phase in SI Fig. S8 is indeed a Li-excess layered phase, which forms as a metastable phase at that composition when phase separation cannot occur fast enough. This trend clearly contrasts with the stoichiometric $LiMnO_2$ composition, in which the orthorhombic phase is the ground state (SI Fig. S9). We note that these sets of enumerated Li-excess structures are not exhaustive, so there may be other possible orderings of each phase that are not considered.

 This journal is © The Royal Society of Chemistry 2026

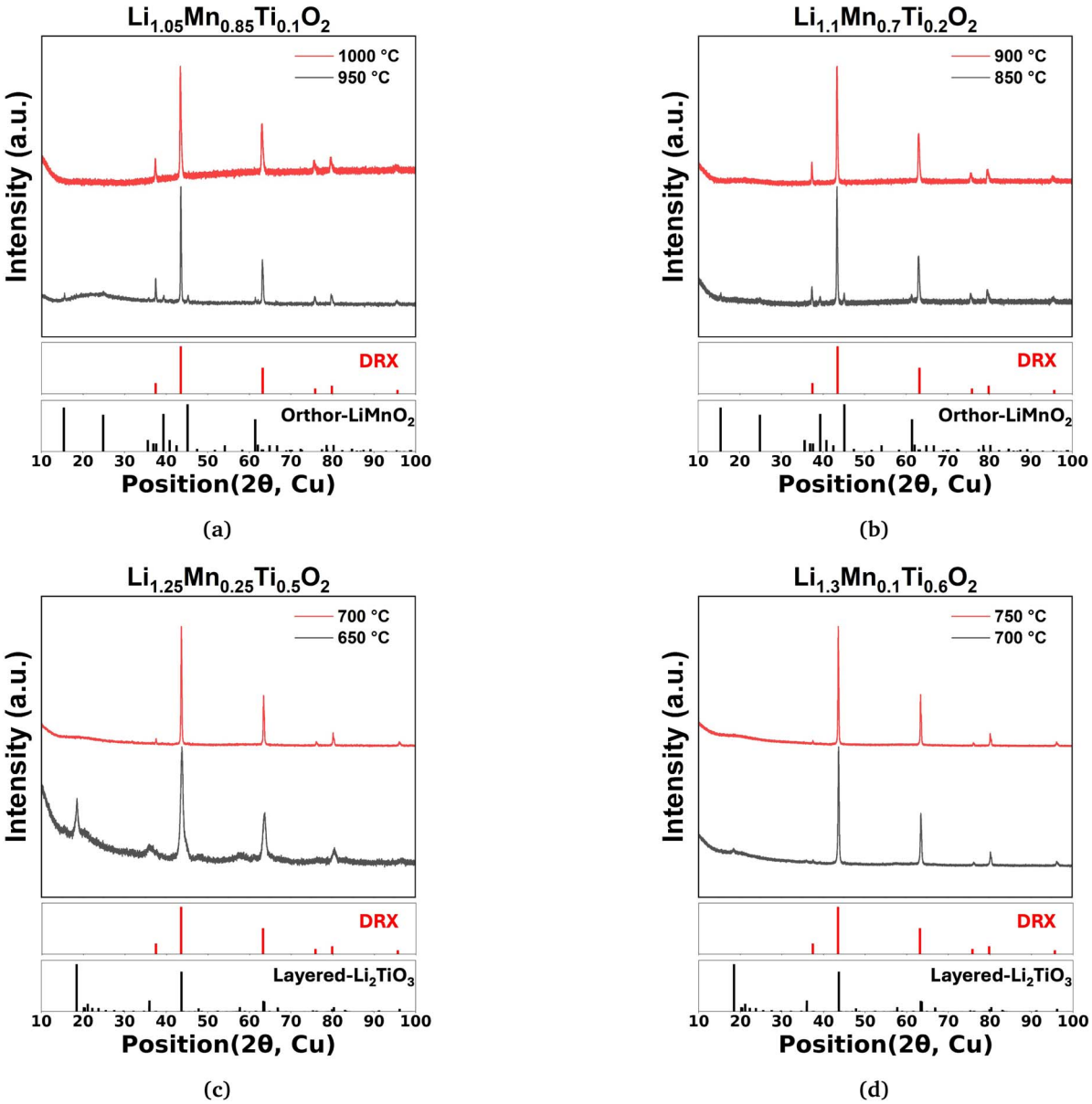


Fig. 4 *Ex situ* XRD patterns of samples quenched from various temperatures. (a) $Li_{1.05}Mn_{0.85}Ti_{0.1}O_2$, (b) $Li_{1.1}Mn_{0.7}Ti_{0.2}O_2$, (c) $Li_{1.25}Mn_{0.25}Ti_{0.5}O_2$, and (d) $Li_{1.3}Mn_{0.1}Ti_{0.6}O_2$, each quenched from temperatures above (red) and below (black) their respective T_{disord}.

To understand the difference between using Ti^{4+} or Mn^{4+} to accommodate Li-excess, we similarly calculate E_{hull} of the orthorhombic, layered, and spinel phases at the $Li_{1.0625}Mn_{0.8125}Ti_{0.125}O_2$ composition, which is plotted in Fig. 6b. These structures also have energies above the convex hulls with $E_{hull} \geq 12$ meV per atom, though these values are on average lower than the $Li_{1.0625}Mn_{0.9375}O_2$ structures (Fig. 6a). For the $Li_{1.0625}Mn_{0.8125}Ti_{0.125}O_2$ composition, the orthorhombic phase is the more energetically favorable as it contains the lowest energy orderings, followed by the layered and spinel phases (Fig. 6b).

These computed energies suggest that for Li-excess compositions along $Li_{1+x}Mn^{3+}_{1-3x}Mn^{4+}_{2x}O_2$, the layered phase is metastable against phase separation but more energetically favorable compared to the orthorhombic phase, and as such, can be stabilized by quenching. Since these computed energies do not include entropic effects, we perform additional canonical MC simulations to calculate the free energy of the Li-excess layered phase at temperatures up to 800 °C, but find that the free energy always lies above the convex hull (SI Fig. S10). The predicted metastability of the layered phase suggests that the layered phase observed in experiment (SI Fig. S8) is a kinetic product that can more rapidly form than the fully phase-separated state, possibly because it requires no long-range diffusion. Upon doping with Ti^{4+}, the Li-excess layered phase is not found in our experiments on $Li_{1+x}Mn^{3+}_{1-3x}Ti^{4+}_{2x}O_2$ samples possibly because the orthorhombic phase is more energetically

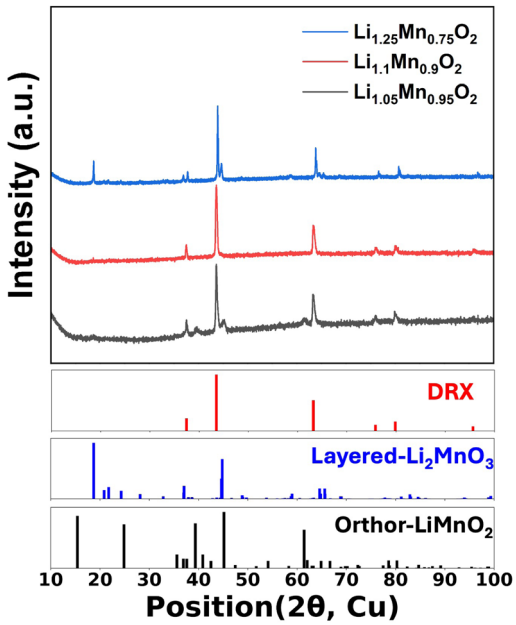


Fig. 5 *Ex situ* XRD patterns of compositions $Li_{1.05}Mn_{0.95}O_2$, $Li_{1.1}Mn_{0.9}O_2$, and $Li_{1.25}Mn_{0.75}O_2$, each quenched from 1100 °C.

favorable compared to the layered phase within this composition range.

3 Discussion

Through a combined first-principles and experimental approach, we have mapped the phase diagram of the LMTO rock-salt phases. We have closely analyzed the $Li_{1+x}Mn^{3+}_{1-3x}Ti^{4+}_{2x}O_2$ ($LiMnO_2$–Li_2TiO_3), ($LiMnO_2$–Li_2MnO_3), and $Li_{1+x}Mn^{3+}_{1-3x}Mn^{4+}_xTi^{4+}_xO_2$ ($LiMnO_2$–$Li_2Mn_{0.5}Ti_{0.5}O_3$) pseudo-binary phase diagrams (Fig. 3), each of which are are eutectoid-like, in which the order-disorder transition temperature (T_{disord}) decreases as off-stoichiometry is introduced to the end-point compositions (adding excess Li to $LiMnO_2$ or Li deficiency to $Li_2D^{4+}O_3$, where D can be Mn, Ti, or an admixture of both). The strong dependence of T_{disord} on composition reveals that the optimization of DRX composition and synthesis temperature are intrinsically coupled. Through heating and *in situ* XRD experiments in an inert atmosphere, we determine the T_{disord} of specific LMTO compositions, which agree reasonably well with the calculated values, though they can deviate by up to ~200 °C.

We interpolate the calculated pseudo-binary phase diagrams to present a schematic pseudo-ternary phase diagram in Fig. 7 at temperatures ranging from 800 to 1100 °C, which spans temperatures below and above conventional DRX synthesis temperatures (~1000 °C). The experimentally verified compositions that form a pure DRX phase at each temperature are also marked in SI Fig. S13. Our simulations suggest that DRX competes with two other phases, which are orthorhombic $LiMnO_2$ and layered $Li_2D^{4+}O_3$, at the temperatures considered (800–1300 °C). The layered $Li_2D^{4+}O_3$ phase (green line in Fig. 7) forms a full solid-solution between Li_2MnO_3 and Li_2TiO_3 (SI Fig. S11). In

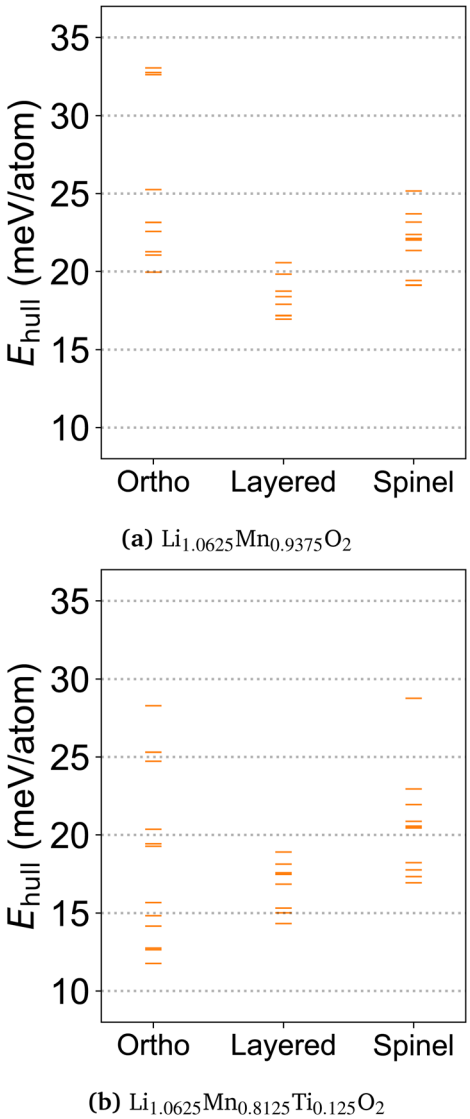


Fig. 6 Energy above the hull (E_{hull}) of Li-excess orthorhombic (ortho), layered, and spinel structures at the (a) $Li_{1.0625}Mn_{0.9375}O_2$ and (b) $Li_{1.0625}Mn_{0.8125}Ti_{0.125}O_2$ compositions, computed from DFT at $T = 0$ K.

experiments, quenched samples of certain compositions contain layered $LiMnO_2$-like impurity phases as well (SI Fig. S8), which our calculations suggest to be metastable when phase separation does not occur. At 800 °C (Fig. 7a), DRX is predicted to be stable only in a small range of compositions with moderate concentration of Li-excess and Ti^{4+} (grey shaded regions in Fig. 7), while the other compositions lie within a multi-phase region (unshaded areas). By 900 °C, the composition range of DRX increases significantly, especially in the Ti^{4+}-rich regions (near the $LiMnO_2$–Li_2TiO_3 pseudo-binary). As temperature increases to 1100 °C, DRX is stable within nearly the entire $LiMnO_2$–Li_2TiO_3 composition space, except in the regions with very little Li-excess, while it is only stable within a limited region within $LiMnO_2$–Li_2MnO_3. Thus, there is an increasing width of the miscibility gap between DRX and $Li_2D^{4+}O_3$ as the ratio of Mn^{4+} to Ti^{4+} increases. These

This journal is © The Royal Society of Chemistry 2026

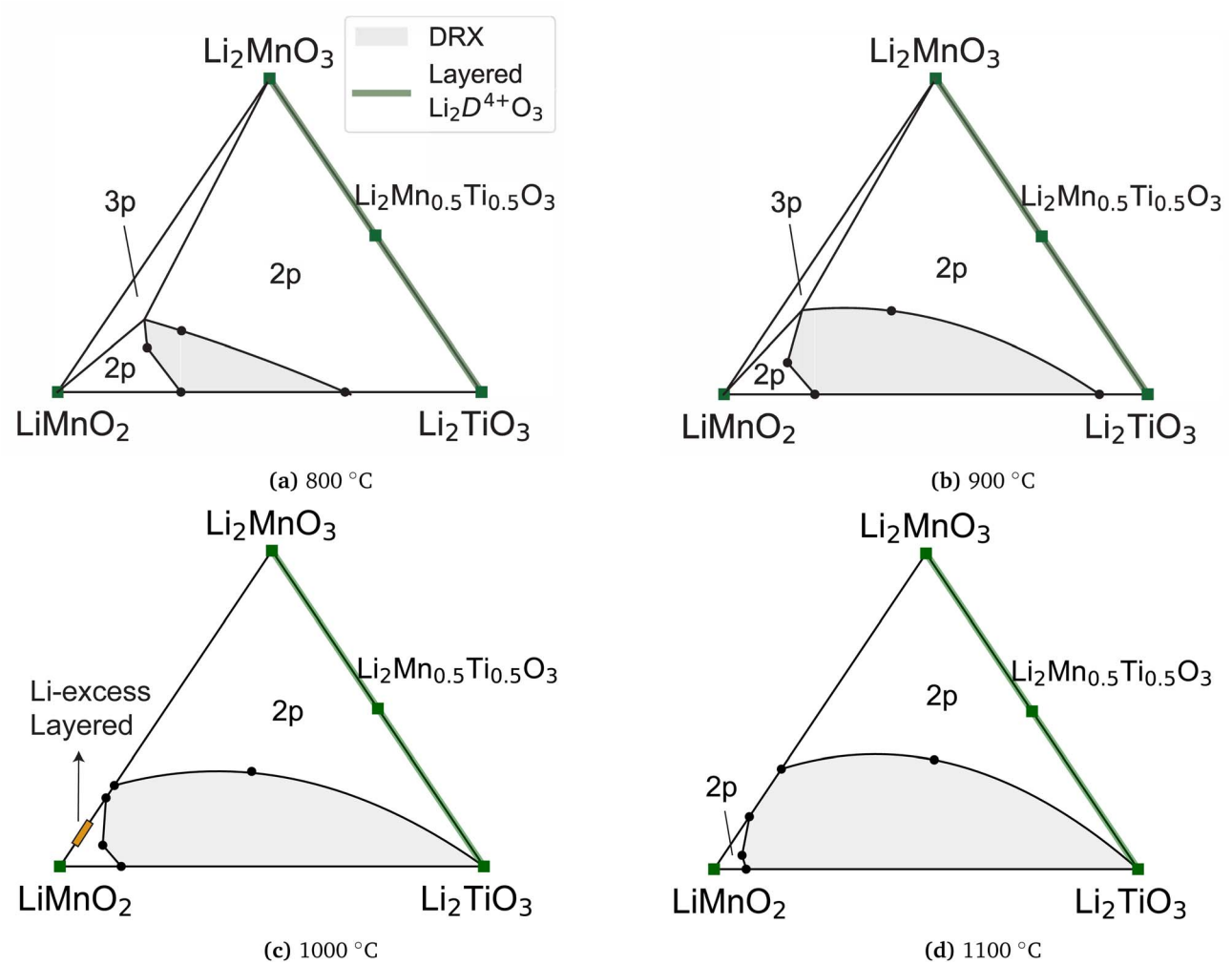


Fig. 7 Pseudo-ternary phase diagram of $LiMnO_2$–Li_2MnO_3–Li_2TiO_3 at (a) 800, (b) 900, (c) 1000, and (d) 1100 °C. The two-phase and three-phase regions are labeled as 2p and 3p, respectively. Black points are obtained from the calculated pseudo-binary phase diagrams (Fig. 3) and the lines are interpolations between them. Gray shaded regions are DRX, green lines represent layered $Li_2D_4{}^+O_3$, and the orange line in (c) denotes the Li-excess layered phase observed in experiment, which our calculations predict to be metastable.

trends are verified by our experimental determination of T_{disord} along $Li_{1+x}Mn^{3+}_{1-3x}Ti^{4+}_{2x}O_2$ and $Li_{1+x}Mn^{3+}_{1-3x}Mn^{4+}_{2x}O_2$ (Fig. 3).

The distinct impact of Ti^{4+} and Mn^{4+} on the thermodynamic accessibility of DRX can be attributed to the differences in electronic structure. Ti^{4+} has negligible filling of d-shell states (d^0), while Mn^{4+} contains d-shells that are partially filled. It was shown by Urban *et al.* that, compared to TM species with d-shells that are (partially) filled, ions with the d^0 electronic structure can better stabilize disordered configurations, as the local lattice distortions that are inherently present in disordered configurations can be accommodated with minimal energy cost.[21] These differences in electronic structure rationalize why the T_{disord} tends to increase significantly as the ratio of Mn^{4+} to Ti^{4+} increases. Notably, the layered Li_2MnO_3 structure is predicted from MC simulations to have a remarkably high T_{disord} > 2800 °C—which may not be realistic as this method does not account for potential melting or reduction, which would occur before reaching such a high temperature. Nevertheless, the high predicted T_{disord} reflects the steep energy cost to disorder the layered Li_2MnO_3 structure. Thus, compositions with substantial Mn^{4+} content favor phase separation into layered Li_2MnO_3 (or $Li_2D^{4+}O_3$ with high Mn^{4+} content), substantially limiting the DRX composition range that is accessible at reasonable temperatures. These results rationalize why there have been few reports of d^0-free and Mn-rich DRX synthesized without the utilization of high-energy mechano–chemical milling techniques.[17,57]

Meanwhile, layered Li_2TiO_3 has a much lower predicted T_{disord} of 1000 °C, reflecting a lower energy cost to disorder. The significantly lower T_{disord} of layered Li_2TiO_3 has pivotal implications, as it implies that the compositions with moderate to high fraction of Ti^{4+} can disorder at much lower temperatures. Specifically, a significant composition range of DRX is stable at temperatures of 800–900 °C, suggesting the potential of lowering the synthesis temperature of many DRX compositions below the conventionally used temperatures ≥1000 °C.[6,8] At 900 °C, DRX within the $Li_{1+x}Mn^{3+}_{1-3x}Ti^{4+}_{2x}O_2$ space is predicted to be stable in the range of Li-excess fraction (x) spanning 0.07–0.28, while in

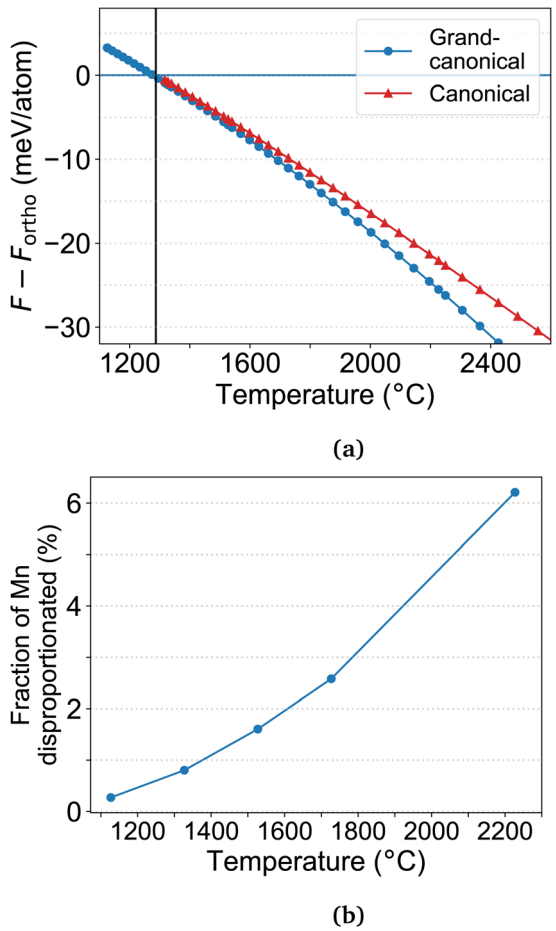


Fig. 8 Free energies (F) and Mn disproportionation of DRX $LiMnO_2$ as a function of temperature in MC simulations using a 5-component CE model containing Li^+, Ti^{4+}, Mn^{2+}, Mn^{3+}, and Mn^{4+}. (a) F relative to ortho-$LiMnO_2$ (F–F_{ortho}) computed within the grand-canonical (GC) and canonical ensembles. GC allows for Mn disproportionation, while canonical maintains Mn in the +3 state only. Vertical line at 1280 °C marks where DRX intersects with ortho-$LiMnO_2$, thus the T_{disord}. (b) Fraction of Mn disproportionated in DRX $LiMnO_2$ within GCMC simulations.

$Li_{1+x}Mn^{3+}_{1-3x}Mn^{4+}_xTi^{4+}_xO_2$ it is stable for x spanning 0.07–0.14 (Fig. 3). The accessible composition range of DRX shrinks significantly as the temperature decreases to 800 °C, but an appreciable portion remains (Fig. 7). Lowering the synthesis temperature is instrumental towards lowering the synthesis energy cost and the ability to optimize DRX particle size, which is subject to rapid coarsening at high temperature, thereby reducing rate performance.[6] Although we predict and verify from experiments that certain compositions have reasonably low T_{disord}, we find that some samples such as $Li_{1.05}Mn_{0.95}O_2$ quenched from above the identified T_{disord} are not pure DRX (Fig. 5). This is likely due to the quench not being fast enough to retain the high-temperature state. Thus, it is essential to develop synthesis methods that can rapidly cool samples with precise temperature control, so samples spend minimal time within two-phase regions.

It is important to note that some compositions containing an admixture of Mn^{4+} and Ti^{4+} can also have reasonably low T_{disord}. This is exemplified by our prediction of $T_{disord} \approx 800$ °C for compositions near $Li_{1.1}Mn_{0.7}{}^{3+}Mn_{0.1}{}^{4+}Ti_{0.1}{}^{4+}O_2$ (Fig. 3c). In fact, the simulated phase boundary of DRX in the $Li_{1+x}Mn^{3+}_{1-3x}Mn^{4+}_xTi^{4+}_xO_2$ phase diagram (Fig. 3c) is nearly identical to the one in $Li_{1+x}Mn^{3+}_{1-3x}Ti^{4+}_{2x}O_2$ (Fig. 3a) at relatively small fractions of Li-excess ($x \leq 0.1$). To our knowledge, these compositions containing both Ti^{4+} and Mn^{4+} have not been previously reported, and thus constitute a relatively new design space in which LMTO DRX can be explored and optimized. The (partial) substitution of Ti^{4+} with Mn^{4+} is potentially important as Wu *et al.* have recently shown that Mn-rich DRX compositions without Ti can yield higher energy density compared to compositions containing Ti, given the same Li concentration.[57] These observations suggest that an optimal balance between thermodynamic accessibility and electrochemical performance can be found by tuning the fraction of Mn^{4+} and Ti^{4+}, especially near Li fractions ≈1.05 to 1.1. Although the full replacement of Ti^{4+} with Mn^{4+} generally yields higher T_{disord}, our calculations predict that the Ti-free DRX composition ≈ $Li_{1.08}Mn_{0.92}O_2$ has a relatively accessible T_{disord} ~1000 °C, as this is the eutectoid point of $Li_{1+x}Mn^{3+}_{1-3x}Mn^{4+}_{2x}O_2$.

We note that many previous studies have incorporated fluorine (F) into the anion sublattice of DRX, which could impact the T_{disord}.[7] In a recent study, Liang *et al.* applied *in situ* XRD to determine the T_{disord} of F-doped $Li_{1.1}Mn_{0.8}Ti_{0.1}O_{1.9}F_{0.1}$ to be ~1000 °C,[56] which is close to our experimentally determined T_{disord} of $Li_{1.05}Mn_{0.85}Ti_{0.1}O_2$ (~960 °C), which contains the same fraction of Ti. Given this close agreement of T_{disord}, we do not expect that the T_{disord} of compositions containing a small fraction of F would deviate far from our results. It should also be noted that one study has questioned whether any significant F incorporation occurs when the Mn content is very high.[58]

In general, our first-principles and experimental phase diagram are in reasonable agreement with each other. Specifically, the predicted changes of T_{disord} with composition agree qualitatively with experiment. However, the quantitative agreement is lacking in some regions of the phase diagram, as the simulated T_{disord} can significantly deviate from the experimental values by up to 150–200 °C, for example at the $LiMnO_2$ and Li_2TiO_3 compositions. The predicted T_{disord} tends to be more accurate for intermediate compositions along $Li_{1+x}Mn^{3+}_{1-3x}Ti^{4+}_{2x}O_2$ and $Li_{1+x}Mn^{3+}_{1-3x}Mn^{4+}_{2x}O_2$, as they are typically within 100 °C of the experimental values. For $Li_{1+x}Mn^{3+}_{1-3x}Ti^{4+}_{2x}O_2$,-experiments yield a eutectoid composition ≈$Li_{1.2}Mn_{0.4}Ti_{0.4}O_2$, which contains higher Li concentration compared to the calculated eutectoid composition ($Li_{1.14}Mn_{0.58}Ti_{0.28}O_2$), though the predicted eutectoid temperature (700 °C) is in close agreement with experiment (~680 °C). In experiments we also find layered $LiMnO_2$-like phases, specifically along the $Li_{1+x}Mn^{3+}_{1-3x}Mn^{4+}_{2x}O_2$ pseudo-binary, that are not predicted to be thermodynamically stable within our simulations.

The methods that we employ capture only configurational excitations, while neglecting the vibrational (S_{vib}) and magnetic (S_{mag}) entropy contributions that are also present in this system, potentially rationalizing the difference between theory and

 This journal is © The Royal Society of Chemistry 2026

experimental results. It has been previously shown that the S_{vib} and its coupling to configurational degrees of freedom can significantly affect predicted T_{disord} and/or solubility limits within alloys.[59,60] While not always the case, the incorporation of vibrational entropy often shifts calculated order-disorder transitions down. The coupling between S_{vib} and S_{config} has been modeled for simple binary systems using the CE approach,[59] but capturing these effects within our higher dimensional quaternary LMTO system would require far greater computational complexity. Magnetic entropy is also present within the LMTO phases, as the orthorhombic $LiMnO_2$ and layered Li_2MnO_3 phases are antiferromagnetically ordered below their Néel temperatures (~280 and 40 K, respectively[23,25]), so they are magnetically disordered at the elevated temperatures that we analyze.

Another potential source of error in our predicted phase diagram stems from the DFT method employed to generate the dataset used to train the CE model. The LMTO system contains electronic structure complexities that can be challenging to model from DFT—namely the presence of strongly correlated 3d electronic states and JT distortions of Mn^{3+}. In a recent study, we specifically highlighted the challenges of modeling the phase stability of the $LiMnO_2$ polymorphs within DFT, which motivated our selection of the HSE06 hybrid-GGA functional in this study, despite its relatively high computational cost.[48] Specifically, HSE06 can accurately predict orthorhombic $LiMnO_2$ to be the ground state, while more commonly used GGA + U and r^{2}SCAN approaches predict a spurious $LiMnO_2$ ground state.[48] It was also shown that the energy differences between phases is highly sensitive to the DFT method used, which indicates that the predicted T_{disord} could possibly be improved by using even more accurate electronic structure methods.

Another potential contribution to the free energy that we have not yet considered is the presence of Mn^{2+}. It is possible for Mn^{2+} to be present within octahedral environments in the rock-salt framework, given that MnO is a known stable phase.[61] Mn^{2+} can form in the LMTO system from the following disproportionation reaction (eqn (1)).

$$2Mn^{3+} \rightleftharpoons Mn^{2+} + Mn^{4+} \quad (1)$$

To investigate the potential influence of Mn^{2+}, we train an additional 5-component CE model that includes Mn^{2+} as a possible species. To train this model, we augment our DFT training structure set to span the MnO–Li_2MnO_3–Li_2TiO_3 space (more details in Methods). We calculate the free energy curves of DRX $LiMnO_2$ from MC simulations within the canonical ensemble containing Mn only in +3 state ($LiMn^{3+}O_2$) and charge–neutral GC ensemble (at fixed chemical potentials) that allows for Mn^{3+} disproportionation to form Mn^{2+} and Mn^{4+} as well. These calculated free energies of DRX relative to the orthorhombic $LiMnO_2$ phase are shown in Fig. 8a. Within these simulations, the predicted T_{disord} of $LiMnO_2$ is predicted to be 1280 °C, regardless whether Mn disproportionation is accounted for. We track the simulated concentration of Mn^{2+} as a function of temperature in Fig. 8b, and find that a relatively small fraction of Mn are disproportionated (<2%) at temperatures below 1600 °C. The low fraction of disproportionation events at these elevated temperatures suggests that the energy cost for Mn disproportionation is substantial. Thus, the additional S_{config} of accounting for Mn^{2+}, in addition to Mn^{3+} and Mn^{4+}, is predicted to be minimal at common DRX synthesis temperatures, so we do not expect it to significantly affect the phase boundaries at typical synthesis temperatures.

4 Conclusions

A phase diagram of the LMTO rock-salt ($LiMnO_2$–Li_2MnO_3–Li_2TiO_3) phase space has been derived from first-principles statistical mechanics calculations and XRD experiments. The LMTO phase diagram is identified to be a eutectoid phase diagram, in which the T_{disord} decreases as off-stoichiometry is introduced to the end-point compositions. Importantly, this leads to a significant range of compositions with T_{disord} ranging from 680–900 °C, which is much lower than conventional DRX synthesis temperatures (≥1000 °C). This finding suggests the potential for lowering synthesis temperature for specific DRX compositions, which can aid in the optimization of particle size/morphology, and in turn the electrochemical performance of LMTO DRX.

5 Experimental

5.1 Theory

All structural enumerations and analysis were performed using the `pymatgen` package.[53,62] To compute the total energy of each enumerated LMTO rock-salt structure, we perform density-functional theory (DFT) calculations using a plane-wave basis set and the projector augmented wave (PAW) method, as implemented in the Vienna *ab initio* Simulation Package (VASP).[63–65] All reported total energies are computed using the HSE06 hybrid generalized gradient approximation (GGA).[49] Since HSE06 requires significantly higher computational cost than the more commonly utilized GGA and *meta*-GGA functionals, we calculate the total energy of each structure using HSE06 at the structural geometries optimized at the *meta*-GGA level (r^{2}SCAN[45]). Specifically, we harness the `atomate2` package[66] to perform a three-step workflow involving the following sequential steps: (1) structural relaxation within GGA (PBEsol + U,[44] where U = 3.9 eV) functional, (2) structural relaxation within r^{2}SCAN + U (U = 1.8 eV), and (3) static calculation of the total energy using HSE06, where U are rotationally averaged Hubbard U corrections[46] on Mn − 3d electron states that were empirically fitted in previous studies to optimize prediction of Mn oxidation reaction enthalpies.[67,68] The initial relaxation using PBEsol + U effectively speeds up the r^{2}SCAN + U relaxation. Although this approach does not calculate each structure's true ground state energy within HSE06, we find that the energy differences between select $LiMnO_2$ phases are reasonably consistent with fully self-consistent HSE06 calculations, with a root mean squared error (RMSE) ~1 meV per atom, which is within the error range of the cluster expansion (SI Fig. S6). We estimate that this workflow reduces the computation time by at least a factor of 5 compared to full relaxations

using HSE06. More details of the DFT calculations are described in SI Note 1.

We use these DFT-computed structures and energies to parametrize a quaternary CE to describe the energies of possible cation orderings of the cubic rock-salt lattice ($Fm\bar{3}m$), with a primitive cell lattice parameter $a = 2.97$ Å. The CE represents the total energy of any configuration as a summation over energy contributions from local cluster interactions.[33,35] We construct our CE model with pair, triplet, and quadruplet cluster interactions up to cluster distances of 8.91, 5.94, and 5.15 Å, respectively, using the `smol` python package, which is also used for all lattice Monte Carlo (MC) simulations.[34] Mixed ℓ_1 and ℓ_2 norm penalized linear regression (Elastic Net[69]), as implemented in the `scikit-learn` package,[70] is used to fit the CE on the DFT energies of 745 unique structures, where the ℓ_1 and ℓ_2 regularization terms promote sparsity and smaller magnitudes of the interactions, respectively. The fit is performed with sample weights applied on the ground state structures and select low-energy structures, a procedure that enables the trained model to correctly preserve the DFT ground states. The 5-fold cross-validation (CV) and training errors of the parametrized CE model are 9.5 meV per atom and 8.5 meV per atom, respectively. The training curves for regularization hyperparameter optimization and further details of CE fitting are shown in SI Fig. S14 and SI Note 2. The CE predicts the correct energy ordering among the orthorhombic, layered, spinel, and γ $LiMnO_2$ phases (SI Fig. S9), which further helps validate the model's accuracy. To understand the influence of Mn^{2+}, we train an additional CE model that describes a quinary cation site space containing Li^+, Mn^{2+}, Mn^{3+}, Mn^{4+}, and Ti^{4+} as possible species. This model was trained in a similar fashion as the quaternary model, with more details described in SI Note 2.

Using the quaternary CE model, we perform MC simulations and thermodynamic integration to calculate the free energies of each phase and determine the phase boundaries between them. For the $Li_{1+x}Mn^{3+}{}_{1-3x}Ti^{4+}_{2x}O_2$ and $Li_{1+x}Mn^{3+}_{1-3x}Mn^{4+}_{2x}O_2$ pseudo-binary spaces, we perform charge–neutral grand-canonical (GC)-MC simulations[71] over a range of temperature (T) and chemical potentials (μ), the details of which are described in SI Note 2. From these MC trajectories, we perform thermodynamic integration over ensemble-averaged energies and compositions to determine the GC free energy (Ω) of the ortho $LiMnO_2$, DRX, layered Li_2TiO_3, and layered Li_2MnO_3 phases. The T and μ values where two Ω curves intersect are identified to determine the boundary between the two phases. To calculate Ω, the average GC energy ($\langle \varepsilon - \mu N \rangle$) is integrated over inverse thermal energy $\left(\beta \equiv \frac{1}{k_B T}\right)$ at a fixed reference μ_0, as described by eqn (2).[72] The μ dependence of Ω is obtained by integrating the average composition ($\langle N \rangle$) over μ at fixed β (eqn (3)).

$$\beta\Omega(\beta,\mu_0) - \beta_0\Omega(\beta_0,\mu_0) = \int_{\beta_0}^{\beta} \langle \varepsilon - \mu_0 N \rangle \mathrm{d}\beta, \text{ at fixed } \mu_0 \quad (2)$$

$$\Omega(\beta,\mu) - \Omega(\beta,\mu_0) = -\int_{\mu_0}^{\mu} \langle N \rangle \mathrm{d}\mu, \text{at fixed } \beta \quad (3)$$

The reference values of μ_0 and β_0 are chosen such that the GC-MC simulations at μ_0 and β_0 equilibrate to the phase of interest. The reference values of β_0 for the ordered phases (ortho $LiMnO_2$, layered Li_2TiO_3, and layered Li_2MnO_3) are chosen at corresponding T_0 below their respective T_{disord}. Meanwhile, β_0 of DRX is chosen to be the $T \to \infty$ limit (equivalently the $\beta \to 0$ limit), where the free energy can be analytically determined through the expression $\beta_0\Omega(\beta_0, \mu_0) = -\ln(\sigma)$,[72] where σ is the number of unique arrangements of the LMTO lattice (*i.e.* $-S_{\text{config}}/k_B$ in the random limit). For a quaternary alloy, this can be trivially evaluated as $\ln(\sigma) = \ln 4$. However, this expression is not valid for the ionic LMTO system, as it accounts for configurations with compositions that are not charge neutral. σ can also be evaluated analytically for a finite supercell of N cation sites and composition defined by n_{Li}, n_{Mn_3}, n_{Mn_4}, and n_{Ti_4} (where n_{Li} is the number of Li, *etc*) by the expression shown in eqn (4a). To facilitate evaluating $\ln(\sigma)$, we apply Stirling's approximation, as shown in eqn (4b), which converges quickly with N.

$$\sigma = \frac{N!}{n_{\text{Li}}!\, n_{\text{Mn}_3}!\, n_{\text{Mn}_4}!\, n_{\text{Mn}_4}!} \quad (4a)$$

$$\ln(\sigma) \approx N\ln(N) - n_{\text{Li}}\ln(n_{\text{Li}}) - n_{\text{Mn}_3}\ln(n_{\text{Mn}_3}) - n_{\text{Mn}_4}\ln(n_{\text{Mn}_4}) - n_{\text{Ti}_4}\ln(n_{\text{Ti}_4}) \quad (4b)$$

σ is thus a function of composition, but in the limits of infinite T and N, the composition will converge to the composition that maximizes S_{config} and in turn σ. Therefore, we perform a GC-MC simulation at $T = 58\,000$ K and $N = 720$, which converges to an average composition $\approx Li_{1.2}Mn_{0.4}{}^{3+}Mn_{0.2}{}^{4+}Ti_{0.2}{}^{4+}O_2$. At this composition, we evaluate using eqn (4b) $\ln(\sigma) \approx 1.089\ k_B$/cation, which importantly is ≈ 21% lower than the corresponding value for a quaternary alloy ($\ln 4 = 1.386\ k_B$/cation), with the reduction in entropy arising from charge neutrality constraints.

We calculate the ≈21% pseudo-binary phase diagram using canonical MC simulations and the common tangent construction. The canonical free energy of DRX (F_{DRX}) is computed at compositions x ranging from 0 to 0.3 in increments of 0.025 along $Li_{1+x}Mn^{3+}_{1-3x}Mn^{4+}_{x}Ti^{4+}_{x}O_2$. The free energy integration scheme to calculate F_{DRX} is identical to the calculation of Ω_{DRX} in the limit of $\mu_0 = 0$ and fixed composition (eqn (2)). The details of the free energy profiles and common tangent construction are shown in SI Fig. S12.

5.2 Experiment

To investigate the disorder temperatures of $Li_{1+x}Mn^{3+}_{1-3x}Mn^{4+}_{2x}O_2$ (x = 0.05, 0.1, 0.15, 0.2, 0.25, 0.3), Li_2CO_3 (Sigma, 99%), Mn_2O_3 (Sigma, 99%) and MnO_2 (Alfa Aesar, 99.9%) were used as precursors. For the $Li_{1+x}Mn_{1-3x}{}^{3+}Ti^{4+}_{2x}O_2$ series (x = 0.05, 0.1, 0.15, 0.2, 0.25, 0.3), Li_2CO_3 (Sigma, 99%), Mn_2O_3 (Sigma, 99%) and TiO_2 (Sigma, 99.5%) were used as precursors. For each composition, a total of 4 g of precursors was stoichiometrically mixed in ethanol using a Retsch PM200 planetary ball mill at 250 rpm for 12 h. A 10% excess of Li_2CO_3 was used to compensate for possible lithium loss during high-temperature treatment. We do not expect this excess lithium

 This journal is © The Royal Society of Chemistry 2026

to significantly alter the stoichiometry of the final DRX phase, as incorporation of additional lithium would require charge compensation, such as oxidation of Mn, which is expected to be limited under an inert atmosphere. The resulting slurry was dried at 70 °C in a convection oven overnight and subsequently ground. Approximately 300 mg of the mixed precursors were pressed into pellets with a diameter of 13 mm.

For *in situ* heating experiments, the pallets were heated to 1100 °C, held at this temperature for 20 min, and then cooled to room temperature using an Anton Paar HTK1200N furnace under a constant nitrogen flow. X-ray diffraction (XRD) data were collected every 10 °C during heating and cooling and continuously collected during holding, using a Bruker D8 Advance diffractometer. All scans were conducted over a 2θ range of 10–70°.

For *ex situ* quenching experiments, pellets were heated to temperatures below and above the respective disorder temperatures and held for 20 min in a tube furnace. The samples were then rapidly removed from the furnace and cooled in ambient air for approximately 1 min using a fan (Milwaukee M12 model, 14 MPH air velocity, 400 CFM airflow rate). The average cooling rate, estimated from the time it took to reach room temperature, was on the order of 10–20 °C s^{-1}. A constant argon flow was maintained throughout the heating process. XRD patterns of the quenched samples were collected using an Aeris Minerals diffractometer (Malvern Panalytical) utilizing Cu Kα radiation. Scans were performed over a 2θ range of 10–100°.

Conflicts of interest

There are no conflicts to declare.

Data availability

The data that support the findings of this study are available from the corresponding author upon reasonable request.

Supplementary information (SI): supporting calculations and experimental data. See DOI: https://doi.org/10.1039/d6ta03748h.

Acknowledgements

We thank Dr Aaron Kaplan for assisting in building the DFT workflow within `atomate2` and Tucker Holstun for insightful discussion about LMTO rock-salt phases. This work was supported by the Assistant Secretary of Energy Efficiency and Renewable Energy, Vehicle Technologies Office of the US Department of Energy (DOE), under contract no. DE-AC02-05CH11231 under the Advanced Battery Materials Research (BMR) Program. S.W. acknowledges partial support from the Jane Lewis Fellowship at UC Berkeley. This research used computational resources of the National Laboratory of the Rockies (NLR) and the National Energy Research Scientific Computing Center (NERSC).

References

1 *Batteries and Secure Energy Transitions, International Energy Agency Technical Report*, 2024.
2 T. Chen, Y. Jin, H. Lv, A. Yang, M. Liu, B. Chen, Y. Xie and Q. Chen, *Trans. Tianjin Univ.*, 2020, **26**, 208–217.
3 F. Maisel, C. Neef, F. Marscheider-Weidemann and N. F. Nissen, *Resour. Conserv. Recycl*, 2023, **192**, 106920.
4 E. A. Olivetti, G. Ceder, G. G. Gaustad and X. Fu, *Joule*, 2017, **1**, 229–243.
5 T. Holstun, T. P. Mishra, L. Huang, H. Hau, S. Anand, X. Yang, C. Ophus, K. Bustillo, L. Ma, S. Ehrlich and G. Ceder, *Adv. Mater.*, 2025, **37**, 2412871.
6 H. Hau, T. Holstun, E. Lee, B. L. D. Rinkel, T. P. Mishra, M. M. DiPrince, R. S. Mohanakrishnan, E. C. Self, K. A. Persson, B. D. McCloskey and G. Ceder, *Adv. Mater.*, 2025, e2502766.
7 R. J. Clément, Z. Lun and G. Ceder, *Energy Environ. Sci.*, 2020, **13**, 345–373.
8 D. Chen, J. Ahn and G. Chen, *ACS Energy Lett.*, 2021, **6**, 1358–1376.
9 H. Li, R. Fong, M. Woo, H. Ahmed, D.-H. Seo, R. Malik and J. Lee, *Joule*, 2022, **6**, 53–91.
10 M. Wang, X. Chen, H. Yao, G. Lin, J. Lee, Y. Chen and Q. Chen, *Energy Environ. Mater.*, 2022, **5**, 1139–1154.
11 H. Ji, A. Urban, D. A. Kitchaev, D.-H. Kwon, N. Artrith, C. Ophus, W. Huang, Z. Cai, T. Shi, J. C. Kim, H. Kim and G. Ceder, *Nat. Commun.*, 2019, **10**, 592.
12 L. Li, B. Ouyang, Z. Lun, H. Huo, D. Chen, Y. Yue, C. Ophus, W. Tong, G. Chen, G. Ceder and C. Wang, *Nat. Commun.*, 2023, **14**, 7448.
13 Z. Cai, H. Ji, Y. Ha, J. Liu, D.-H. Kwon, Y. Zhang, A. Urban, E. E. Foley, R. Giovine, H. Kim, Z. Lun, T.-Y. Huang, G. Zeng, Y. Chen, J. Wang, B. D. McCloskey, M. Balasubramanian, R. J. Clement, W. Yang and G. Ceder, *Matter*, 2021, **4**, 3897–3916.
14 Z. Cai, B. Ouyang, H.-M. Hau, T. Chen, R. Giovine, K. P. Koirala, L. Li, H. Ji, Y. Ha, Y. Sun, J. Huang, Y. Chen, V. Wu, W. Yang, C. Wang, R. J. Clement, Z. Lun and G. Ceder, *Nat. Energy*, 2023, 1–10.
15 S. Patil, D. Darbar, E. C. Self, T. Malkowski, V. C. Wu, R. Giovine, N. J. Szymanski, R. D. McAuliffe, B. Jiang, J. K. Keum, K. P. Koirala, B. Ouyang, K. Page, C. Wang, G. Ceder, R. J. Clement and J. Nanda, *Adv. Energy Mater.*, 2023, **13**, 2203207.
16 J. Ahn, Y. Ha, R. Satish, R. Giovine, L. Li, J. Liu, C. Wang, R. J. Clement, R. Kostecki, W. Yang and G. Chen, *Adv. Energy Mater.*, 2022, **12**, 2200426.
17 H.-M. Hau, T. Mishra, C. Ophus, T.-Y. Huang, K. Bustilo, Y. Sun, X. Yang, T. Holstun, X. Zhao, S. Wang, Y. Ha, G.-H. Lee, C. Song, J. Turner, J. Bai, L. Ma, K. Chen, F. Wang, W. Yang, B. D. McCloskey, Z. Cai and G. Ceder, *Nat. Nanotechnol.*, 2024, **19**, 1831–1839.
18 T. Li, T. S. Geraci, K. P. Koirala, A. Zohar, E. N. Bassey, P. A. Chater, C. Wang, A. Navrotsky and R. J. Clement, *J. Am. Chem. Soc.*, 2024, 24296–24309.

19 D. Chen, J. Wu, J. K. Papp, B. D. McCloskey, W. Yang and G. Chen, *Small*, 2020, **16**, e2000656.
20 V. C. Wu, H. A. Evans, R. Giovine, M. B. Preefer, J. Ong, E. Yoshida, P. Cabelguen and R. J. Clement, *Adv. Energy Mater.*, 2023, **13**, 2203860.
21 A. Urban, A. Abdellahi, S. Dacek, N. Artrith and G. Ceder, *Phys. Rev. Lett.*, 2017, **119**, 176402.
22 G. Dittrich and R. Hoppe, *Z. Anorg. Allg. Chem.*, 1969, **368**, 262–270.
23 J. Greedan, N. Raju and I. Davidson, *J. Solid State Chem.*, 1997, **128**, 209–214.
24 L. Croguennec, P. Deniard, R. Brec and A. Lecerf, *J. Mater. Chem.*, 1995, **5**, 1919–1925.
25 P. Strobel and B. Lambert-Andron, *J. Solid State Chem.*, 1988, **75**, 90–98.
26 A. Boulineau, L. Croguennec, C. Delmas and F. Weill, *Chem. Mater.*, 2009, **21**, 4216–4222.
27 J. Dorrian and R. Newnham, *Mater. Res. Bull.*, 1969, **4**, 179–183.
28 H. Kleykamp, *Fusion Eng. Des.*, 2002, **61**, 361–366.
29 G. Izquierdo and A. R. West, *Mater. Res. Bull.*, 1980, **15**, 1655–1660.
30 E. J. Wu, P. D. Tepesch and G. Ceder, *Philos. Mag. B.*, 1998, **77**, 1039–1047.
31 A. Riou, A. Lecerf, Y. Gerault and Y. Cudennec, *Mater. Res. Bull.*, 1992, **27**, 269–275.
32 X. Li, X. Li, L. Monluc, B. Chen, M. Tang, P. Chien, X. Feng, I. Hung, Z. Gan, A. Urban and Y. Hu, *Adv. Energy Mater.*, 2022, **12**, 2200427.
33 L. Barroso-Luque, P. Zhong, J. H. Yang, F. Xie, T. Chen, B. Ouyang and G. Ceder, *Phys. Rev. B*, 2022, **106**, 144202.
34 L. Barroso-Luque, J. H. Yang, F. Xie, T. Chen, R. L. Kam, Z. Jadidi, P. Zhong and G. Ceder, *J. Open Source Softw.*, 2022, 4504.
35 J. M. Sanchez, F. Ducastelle and D. Gratias, *Phys. Stat. Mech. Appl.*, 1984, **128**, 334–350.
36 J. H. Yang, T. Chen, L. Barroso-Luque, Z. Jadidi and G. Ceder, *npj Comput. Mater.*, 2022, **8**, 133.
37 P. Zhong, T. Chen, L. Barroso-Luque, F. Xie and G. Ceder, *Phys. Rev. B*, 2022, 024203.
38 T. Chen, J. Yang, L. Barroso-Luque and G. Ceder, *ACS Energy Lett.*, 2022, 314–319.
39 Z. Pei, R. Li, M. C. Gao and G. M. Stocks, *npj Comput. Mater.*, 2020, **6**, 122.
40 A. v. d. Walle, M. Asta and G. Ceder, *Calphad*, 2002, **26**, 539–553.
41 R. Drautz and M. Fähnle, *Phys. Rev. B:Condens. Matter Mater. Phys.*, 2004, **69**, 104404.
42 E. Decolvenaere, E. Levin, R. Seshadri and A. V. d. Ven, *Phys. Rev. Mater.*, 2019, **3**, 104411.
43 F. Zhou, T. Maxisch and G. Ceder, *Phys. Rev. Lett.*, 2006, **97**, 155704.
44 J. P. Perdew, A. Ruzsinszky, G. I. Csonka, O. A. Vydrov, G. E. Scuseria, L. A. Constantin, X. Zhou and K. Burke, *Phys. Rev. Lett.*, 2008, **100**, 136406.
45 J. W. Furness, A. D. Kaplan, J. Ning, J. P. Perdew and J. Sun, *J. Phys. Chem. Lett.*, 2020, **11**, 8208–8215.
46 S. L. Dudarev, G. A. Botton, S. Y. Savrasov, C. J. Humphreys and A. P. Sutton, *Phys. Rev. B:Condens. Matter Mater. Phys.*, 1998, **57**, 1505–1509.
47 M. Barré and M. Catti, *J. Solid State Chem.*, 2009, **182**, 2549–2554.
48 R. L. Kam, L. Binci, A. D. Kaplan, K. Persson, N. Marzari and G. Ceder, *Phys. Rev. B*, 2025, **111**, 245132.
49 A. V. Krukau, O. A. Vydrov, A. F. Izmaylov and G. E. Scuseria, *J. Chem. Phys.*, 2006, **125**, 224106.
50 M. Cococcioni and S. d. Gironcoli, *Phys. Rev. B:Condens. Matter Mater. Phys.*, 2004, **71**, 035105.
51 S. K. Mishra and G. Ceder, *Phys. Rev. B:Condens. Matter Mater. Phys.*, 1999, **59**, 6120–6130.
52 M. K. Horton, J. H. Montoya, M. Liu and K. A. Persson, *npj Comput. Mater.*, 2019, **5**, 64.
53 M. K. Horton, P. Huck, R. X. Yang, J. M. Munro, S. Dwaraknath, A. M. Ganose, R. S. Kingsbury, M. Wen, J. X. Shen, T. S. Mathis, A. D. Kaplan, K. Berket, J. Riebesell, J. George, A. S. Rosen, E. W. C. Spotte-Smith, M. J. McDermott, O. A. Cohen, A. Dunn, M. C. Kuner, G.-M. Rignanese, G. Petretto, D. Waroquiers, S. M. Griffin, J. B. Neaton, D. C. Chrzan, M. Asta, G. Hautier, S. Cholia, G. Ceder, S. P. Ong, A. Jain and K. A. Persson, *Nat. Mater.*, 2025, 1–11.
54 J. M. Paulsen and J. R. Dahn, *Chem. Mater.*, 1999, **11**, 3065–3079.
55 Y.-I. Jang, W. Moorehead and Y.-M. Chiang, *Solid State Ionics*, 2002, **149**, 201–207.
56 Z. Liang, O. Marques, O. A. P. Mellone, S. M. Masina, C. L. Cao, D. Sokaras, J. N. Weker and K. H. Stone, *Chem. Mater.*, 2025, **37**, 3950–3958.
57 V. C. Wu, E. A. Lawrence, T. Li, E. N. Bassey, C.-Y. Chang, B. J. Hwang, P.-E. Cabelguen and R. J. Clement, *Energy Environ. Sci.*, 2025, **18**, 8918–8928.
58 V. C. Wu, P. Zhong, J. Ong, E. Yoshida, A. Kwon, G. Ceder and R. J. Clement, *ACS Energy Lett.*, 2024, **9**, 3027–3035.
59 A. v. d. Walle and G. Ceder, *Rev. Mod. Phys.*, 2002, **74**, 11–45.
60 J. Z. Liu, G. Ghosh, A. v. d. Walle and M. Asta, *Phys. Rev. B:Condens. Matter Mater. Phys.*, 2007, **75**, 104117.
61 I. A. Blech and B. L. Averbach, *Phys. Rev.*, 1966, **142**, 287–290.
62 S. P. Ong, W. D. Richards, A. Jain, G. Hautier, M. Kocher, S. Cholia, D. Gunter, V. L. Chevrier, K. A. Persson and G. Ceder, *Comput. Mater. Sci.*, 2013, **68**, 314–319.
63 G. Kresse and J. Furthmüller, *Phys. Rev. B:Condens. Matter Mater. Phys.*, 1996, **54**, 11169–11186.
64 G. Kresse and D. Joubert, *Phys. Rev. B:Condens. Matter Mater. Phys.*, 1998, **59**, 1758–1775.
65 G. Kresse and J. Furthmüller, *Comput. Mater. Sci.*, 1996, **6**, 15–50.
66 A. Ganose, H. Sahasrabuddhe, M. Asta, K. Beck, T. Biswas, A. Bonkowski, J. Bustamante, X. Chen, Y. Chiang, D. Chrzan, J. Clary, O. Cohen, C. Ertural, M. Gallant, J. George, S. Gerits, R. Goodall, R. Guha, G. Hautier, M. Horton, A. Kaplan, R. Kingsbury, M. Kuner, B. Li, X. Linn, M. McDermott, R. S. Mohanakrishnan, A. Naik, J. Neaton, K. Persson, G. Petretto, T. Purcell, F. Ricci, B. Rich, J. Riebesell, G.-M. Rignanese, A. Rosen,

 This journal is © The Royal Society of Chemistry 2026

M. Scheffler, J. Schmidt, J.-X. Shen, A. Sobolev, R. Sundararaman, C. Tezak, V. Trinquet, J. Varley, D. Vigil-Fowler, D. Wang, D. Waroquiers, M. Wen, H. Yang, H. Zheng, J. Zheng, Z. Zhu and A. Jain, *Digital Discovery*, 2025, 1944–1973.

67 L. Wang, T. Maxisch and G. Ceder, *Phys. Rev. B:Condens. Matter Mater. Phys.*, 2006, **73**, 195107.

68 S. Swathilakshmi, R. Devi and G. S. Gautam, *J. Chem. Theory Comput.*, 2023, **19**, 4202–4215.

69 H. Zou and T. Hastie, *J. R. Stat. Soc., Ser. B Stat. Methodol.*, 2005, **67**, 301–320.

70 F. Pedregosa, G. Varoquaux, A. Gramfort, V. Michel, B. Thirion, O. Grisel, M. Blondel, P. Prettenhofer, R. Weiss, V. Dubourg, J. Vanderplas, A. Passos, D. Cournapeau, M. Brucher, M. Perrot and E. Duchesnay, *J. Mach. Learn. Res.*, 2011, **85**, 2825–2830.

71 F. Xie, P. Zhong, L. Barroso-Luque, B. Ouyang and G. Ceder, *Comput. Mater. Sci.*, 2023, **218**, 112000.

72 A. v. d. Walle and M. Asta, *Model. Simulat. Mater. Sci. Eng.*, 2002, **10**, 521.

This journal is © The Royal Society of Chemistry 2026